Finite-Element Simulation of Mixing: 2. Three-Dimensional Flow Through a Kenics Mixer

Th. Avalosse
POLYFLOW s.a., 16 Place de l'Université, 1348 Louvain-la-Neuve, Belgium

M. J. Crochet
Césame Université Catholique de Louvain, 4 avenue G. Lemaître, 1348 Louvain-la-Neuve, Belgium

Numerical tools for the analysis of complex 3-D mixing devices were developed. Calculations are based on the finite-element method. The flow calculation is combined with that of pathlines for a fairly large number of material points; along these pathlines, relevant kinematic variables, which are then subjected to a statistical treatment, are evaluated. These numerical techniques are applied to the analysis of a Kenics mixer. It is assumed that the geometry is periodic in the axial direction, that is, that the mixer contains an infinite number of blades; the finite-element analysis may then be completed on a single wavelength of the geometry. To test the accuracy of the three-dimensional calculation, a Kenics device was mounted in order to mix clays of different colors, and photographs of experimental cross-sections were compared with numerical results showing concentration maps. A statistical treatment was performed on some 8,000 material points crossing the entry section to evaluate mixing quality.

Introduction

In this second article, we pursue the development of numerical tools with a view to the analysis of complex three-dimensional mixing devices. We are aware at the outset that the high computational cost of complex 3-D flows imposes serious restrictions on the type of problems that can be tackled with present computational resources (Avalosse, 1994). The central problem for mixing calculations is accuracy (Souvaliotis et al., 1995); a relatively coarse finite-element mesh may generate acceptable velocity fields, but the computation of pathlines, essential for any mixing calculation, is then severely impaired. The usual symptom of inaccuracy is the loss of material particles through solid walls. While high accuracy can be reached for 2-D viscous-flow problems with appropriate grid refinement, the situation is quite different for complex 3-D shapes such as those encountered in twin-screw extruders.

Our calculations are based on the finite-element method; we solve on purpose a non-Newtonian flow in order to depart from analytical problems. The finite-element flow calculation is combined with that of pathlines for a fairly large number of material points; along these pathlines, we evaluate relevant kinematic variables that are then subjected to a statistical treatment.

The 3-D counterpart to our analysis of co- or counterrotating cam devices in our first article (Avalosse and Crochet, 1997) would be that of co- or counterrotating twin-screw extruders. However, in addition to the accuracy problem just mentioned, 3-D mesh generation in moving domains is at present a major obstacle. It is the reason we limit our analysis to a static mixer. Another problem of interest, relying on a time-independent geometry, was investigated by Tanguy et al. (1992), who studied the flow in a helical mixer, where the selection of a rotating frame of reference allows one to use a fixed geometry. We apply our numerical techniques to the analysis of a Kenics mixer (see, e.g., Middleman, 1977), which was made the object of earlier research. The problem was considered by Khakar et al. (1987) and results based on chaos theory are described in detail by Ottino (1989). These authors base their developments on analytical evaluations of the velocity field in the semicircular cross section. In a recent article, Ling (1995) calculated the flow in an infinitely long element and combined Galerkin and finite difference methods to solve the flow in the axial and in the transverse directions, respectively. Our only simplification here is to assume that the geometry is periodic in the axial direction, that is, that the mixer contains an infinite number of blades. Pro-

vided that mixing does not alter fluid properties, we may then complete the finite-element analysis on a single wavelength of the geometry, with the rule that the velocity field is periodic. In order to test the accuracy of our full 3-D calculation, we have also mounted a Kenics device in order to mix clays of different colors, and we have compared photographs to experimental cross-sections with numerical results showing concentration maps.

The geometry of the flow is described in the next section, together with the hypotheses underlying the calculation. The mixing variables are recalled in the third section, together with the method used for their calculation. The experimental results are shown in the fourth section, and they are compared to finite-element results in the fifth section. The results of the statistical treatment applied to some 8,000 material points are also explained in that section. The accuracy of our calculations is discussed in the sixth.

Geometry of the Flow

We calculate the stationary flow of generalized Newtonian fluids through an open domain (with an entry and an exit section) that is spatially periodic. A typical example is the Kenics mixer shown in Figure 1. The mixer is made of a long tube containing static elements that induce mixing while a pressure loss activates the flow. The static elements are helical blades with alternately clockwise and counterclockwise orientations with respect to the axial direction. The blade connection is such that the ridges of successive blades are orthogonal. In principle, the matter is separated in two parts at every change of blade, as shown in Figure 2 (see Middleman, 1977). A periodic element of the geometry, shown in Figure 3, is made of a half clockwise blade, a full counterclockwise blade, and then another half clockwise blade.

In our mixing analysis, we assume that, in the entry section, the lobes are filled with fluids A and B; they have a different color and they are separated by a straight line that is orthogonal to the ridge. We wish to calculate mixing along the axis, but some assumptions are made at the outset.

1. Both fluids have the same rheological behavior, that is, that of a power-law fluid with a shear viscosity μ given by

$$\mu = K\dot{\gamma}^{n-1}, \tag{1}$$

where $\dot{\gamma}$ is the shear rate, K the consistency factor, and n the power index.

2. The concentration does not affect the flow.
3. The fluids do not react or diffuse.
4. There is no interfacial tension.
5. The flow is isothermal.
6. There is no slip along solid walls.
7. Inertia and body forces are not taken into account.

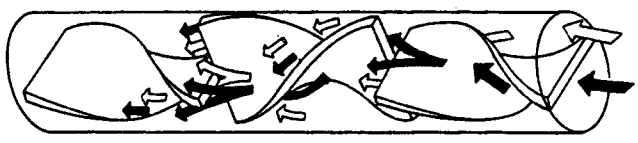

Figure 1. Geometry of the Kenics mixer.

A cylindrical tube contains a succession of twisted blades. (Reprinted with permission from Middleman, 1977.)

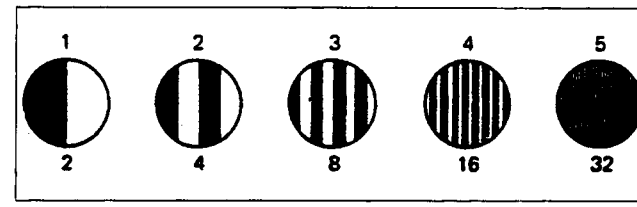

Figure 2. Generation of strias in a "perfect" Kenics mixer; the material is sliced in two parts after every change of blade.

Reprinted with permission from Middleman, 1977.

Under such conditions, we may calculate the flow of a homogeneous fluid through the system and later evaluate the mixing variables. In calculating the flow through a periodic element, we assume that the flow rate is imposed and that the velocity of a material point in the entry section is equal to that of the corresponding point in the exit section. There is a uniform pressure difference between the entry and exit sections. Under such conditions of periodicity, we do not impose a velocity field in the entry section. The only constraint is the flow rate, which in turn determines the pressure gradient. While we use a periodic geometrical element to calculate the flow, we need to combine several successive elements for the mixing calculations, since variables such as area stretch are not spatially periodic and must be calculated throughout the whole mixer.

Mixing Variables

In our previous article (Avalosse and Crochet, 1997) we were interested in the temporal evolution of kinematic variables describing the quality of mixing. In the present steady flow, we calculate the evolution of mixing variables as a function of the axial coordinate z of the outer tube. More precisely, we select a number of material points in the entry section and we follow their path through the mixer in the axial direction. Essentially, we measure the growth of the interface between fluids A and B. For that purpose, we calculate throughout the flow the growth of the area stretch for a num-

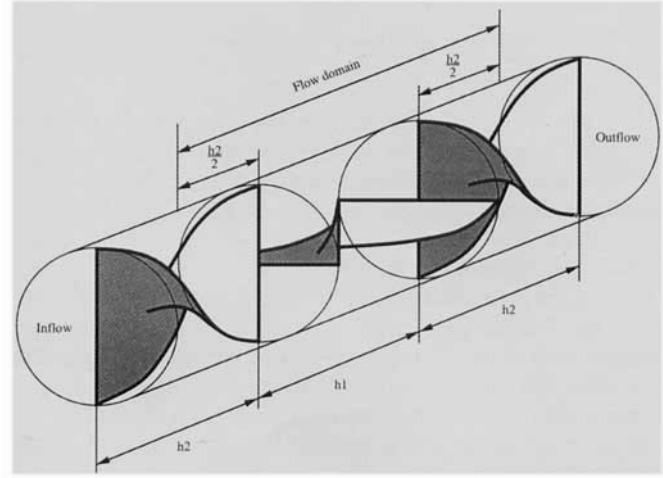

Figure 3. Periodic element in the geometry of the Kenics mixer.

ber of material particles initially located in the entry section, associated with a unit vector normal to the element of area.

Let us combine a material particle in the entry section with an oriented infinitesimal area dA with a unit normal N; at time t, we obtain an infinitesimal area da with a unit normal n. The area stretch η is defined by the ratio da/dA. For an incompressible fluid, it was shown (Ottino, 1989) that

$$\eta = (N \cdot C^{-1} N)^{1/2}, \tag{2}$$

where C is the right Cauchy–Green strain tensor at time t. The normal n at time t is given by

$$n = \frac{(F^{-1})^t N}{\eta}, \tag{3}$$

where F is the deformation gradient tensor.

It was also shown by (Ottino, 1989), that the area stretch η obeys the following inequality,

$$-D \le \dot{\eta}/\eta \le D; \tag{4}$$

the dot stands for the material time derivative, while D is an invariant of the rate of deformation tensor D, that is,

$$D = (trD^2)^{1/2}. \tag{5}$$

The instantaneous area efficiency e_η is thus defined as follows:

$$e_\eta = \frac{\dot{\eta}/\eta}{D}, \tag{6}$$

where e_η indicates the amount of instantaneous rate of deformation used to stretch the element of area da. A positive (negative) value of e_η indicates that the material volume shrinks (stretches) in the normal direction n and that the element of area stretches (shrinks). For an infinitesimal area dA associated with a material point, it is interesting to calculate the time-averaged efficiency, which is defined as follows:

$$\langle e_\eta \rangle = \frac{1}{t} \int_0^t e_\eta(t')\, dt'. \tag{7}$$

Finally, for any material point passing through the mixer, it is useful to calculate its residence time between the entry and the exit sections. The computation of the residence time, together with that of η, e_η, and $\langle e_\eta \rangle$, requires the calculation of pathlines. In our previous article (Avalosse and Crochet, 1997), the calculation was based on the fact that a new finite-element mesh was used for every iteration. In the present article, the calculations proceed on a fixed 3-D mesh. Under such circumstances, we have obtained a better accuracy through the calculation of pathlines in the parent element rather than in the actual element, with the use of the fourth-order Runge-Kutta method (Goublomme et al., 1992; Avalosse, 1994).

For a spatially periodic domain, we must distinguish between the location x of the material point in the reduced domain occupying one wavelength and its position y in the global domain made of several wavelengths. Let $x(t)$ and $y(t)$ denote the values of x and y at time t. As long as x does not reach the exit of the reduced domain, we can write

$$y(t + \delta t) = y(t) + x(t + \delta t) - x(t). \tag{8}$$

When $x(t + \delta t)$ reaches the exit section, we restart the calculation in the reduced domain at

$$x^* = x(t + \delta t) - Le_z, \tag{9}$$

where L is the wavelength and e_z is the axis of the mixer.

To evaluate the mixing variables, we identify m cross sections normal to the axis of the cylindrical boundary associated with the axial coordinate z. In the entry section, we select a grid of material points as we did in the study of 2-D flows (Avalosse and Crochet, 1997). The area stretch receives the unit value, the residence time vanishes, and we select a random orientation N for the element of area associated with every material point. Let us assume that we have obtained a set of material points located in section i, $1 \le i \le m$. We then calculate the pathline of every material point until they reach section $(i + 1)$, and so on until $i + 1 = m$. Again, a fourth-order Runge-Kutta algorithm is used to calculate the deformation gradient F through the relationship

$$\dot{F} = LF, \tag{10}$$

where L is the velocity gradient tensor. The knowledge of F allows us to calculate the mixing variables η, e_η, and $\langle e_\eta \rangle$ in successive cross sections of the mixer and to perform a statistical evaluation.

The accuracy of the calculation is a difficult problem in 3-D flow, where the finite-element meshes are still relatively coarse compared with two-dimensional calculations. Additionally, the mixing parameters in a given cross section i are not all calculated with the same accuracy, which depends on the amount of time needed to travel from the entry section to the cross section under investigation. The faster a particle reaches cross section i, the higher the accuracy of F as calculated by Eq. 10. In 3-D flow, a rough evaluation of accuracy is obtained by counting the number of material points lost between the entry and the exit sections. We will indeed disregard those material points that eventually cross the lateral boundary of the flow domain.

Finally, the present method of calculation allows us to calculate the evolution of concentration in successive cross sections. It is indeed assumed that, in the absence of diffusion and chemical reactions, a material particle keeps the same concentration along its pathline throughout the flow. In later sections, we will assume that a material point receives a given "color" or concentration in the entry section. It is then easy to obtain the color distribution in successive cross sections, and in particular to calculate the segregation scale as described by Avalosse and Crochet (1997).

Experimental Results

In order to compare our numerical results with their experimental counterparts, we have built an easily dismountable

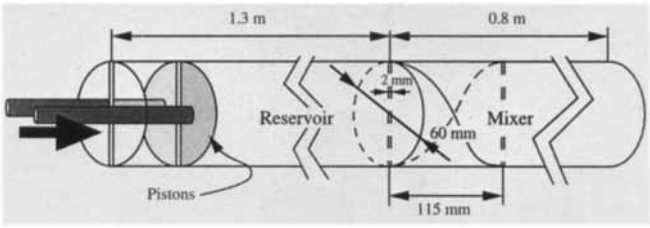

Figure 4. Experimental device.

Kenics mixer to measure along the axis the mixing of different colored clays. The selected fluid was Playstuff clay diluted in 200% of water. For the range of the shear rates of the flow to be calculated, its shear behavior is well represented by a power-law fluid with a power index of 0.4.

The experimental device shown in Figure 4 is made of a reservoir and of the mixer itself. The reservoir is a 1.3-m-long tube with an internal diameter of 60 mm. A 2-mm-thick plate divides the internal volume of the reservoir into two equal volumes containing clays of different colors. The moving system is made of two pistons with a half-circular shape; the pistons are fixed on tied rods such that their axial motion guarantees the same flow rate in both parts of the reservoir. The mixer itself is made of two half-cylinders containing a set of blades. The inner diameter diameter of the cylinder is 60 mm; the length of the mixer is 0.8 m. The system contains seven blades welded to each other; each of them is 0.115 m long, 2 mm thick, and 60 mm wide. The Reynolds number of the flow is of the order of 0.01.

The experiment mixes two clays of the same rheological behavior that are, respectively, green and red. The successive steps are as follows:

1. Each half of the reservoir is filled with a clay of a different color.
2. The reservoir is positioned on the mixer such that the separating plate is orthogonal to the ridge of the first blade.
3. The simultaneous motion of both pistons forces the clay through the mixer until the mixture continuously flows through the exit section.
4. The reservoir is removed from the mixer, which stays in a freezer for 4 hours.
5. The mixer is dismounted; slices of clay are cut perpendicular to the axis, cleaned, and photographed.

Figure 5 shows the mixing progress from the entry section up to the end of the fourth blade, beyond which strias are too thin to be observed. The evolution of the lamellar structure is easily observable; the number of strias doubles after every blade. Along a given blade, the fluid undergoes a rotation as it progresses in the tube; while the strias are essentially orthogonal to the blade on the left of Figure 5, they become essentially parallel to it on the right. We also observe that, in a given cross section, the strias do not all have same thickness. As shown in Figure 6, a less striated zone is visible in one of the corners; similar properties were observed by Middleman (1977).

Numerical Results

In Figure 3 we showed the periodic element of the geometry of the Kenics mixer. We assumed at the outset that the velocity field is periodic as well, and we performed a finite-element calculation in the domain of Figure 3. The finite-element mesh, shown in Figure 7 in its untwisted shape, contains 1,840 brick elements. Each cross section contains 92 plane elements. In our calculations, we use triquadratic elements for the velocity field and trilinear elements for the pressure. There are 50,922 nodal velocity components and 2,436 nodal pressures.

Figure 5. Successive slices of the mixture along the first four blades.

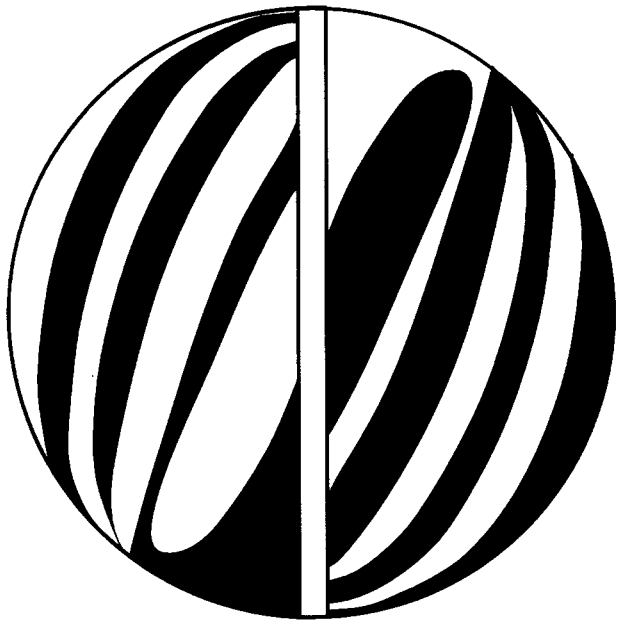

Figure 6. Cross section of the mixture.

We have calculated the flow with two different fluids: a Newtonian fluid and a generalized Newtonian fluid with a power index of 0.4 corresponding to the diluted clay. The flow rate of 37.7 cm^3/s is such that inertia effects can be neglected in the calculation. In Figure 8, we examine the evolution of the velocity field before and after a change of blade located at $z = 0$; we show the projection of the velocity vectors in the x-y plane for the Newtonian fluid and the contourlines of the axial velocity for the Newtonian as well as the generalized Newtonian fluid. We observe, as expected, that the change of blade strongly modifies the velocity distribution. Additionally, a lower number of contourlines for the

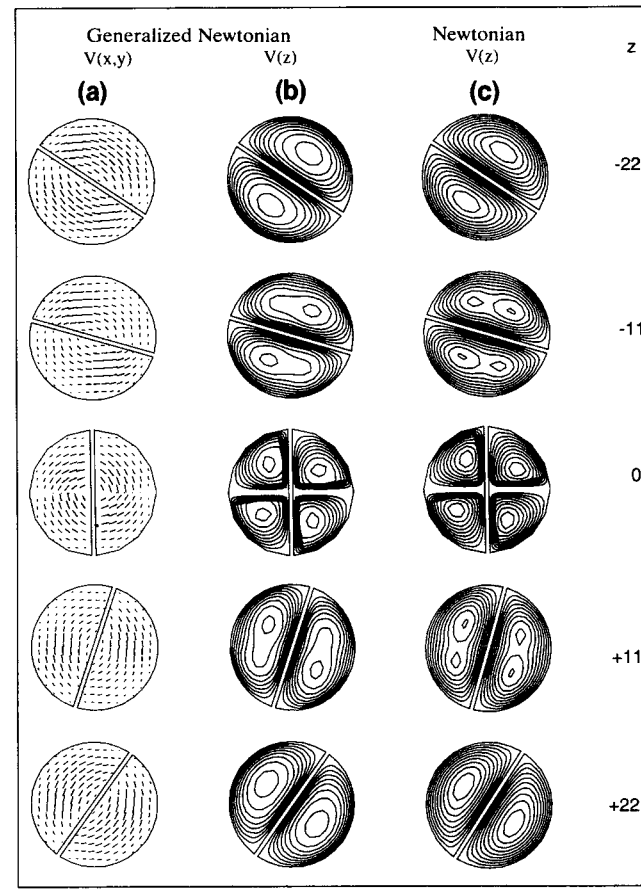

Figure 8. Evolution of the velocity field before and after a change of blade located at $z = 0$.

(a) Projection of the velocity field in the cross section; (b) contour lines of the axial velocity field for the generalized Newtonian fluid; (c) same as (b) for the Newtonian fluid.

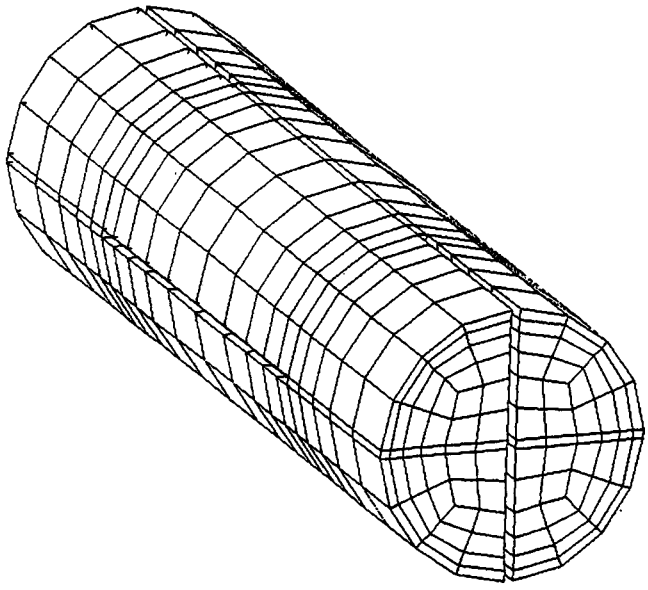

Figure 7. Untwisted finite-element mesh covering the domain of Figure 3.

The mesh contains 1,840 brick elements.

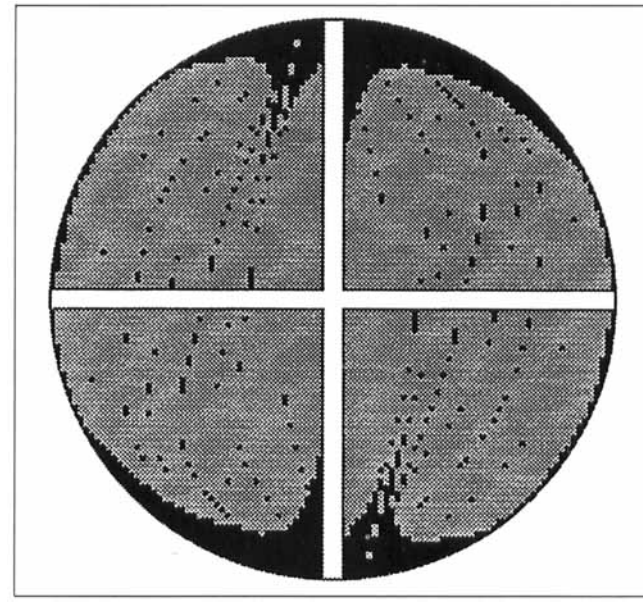

Figure 9. Lost particles in the entry section.

The black region corresponds to particles that will cross the wall and be eliminated.

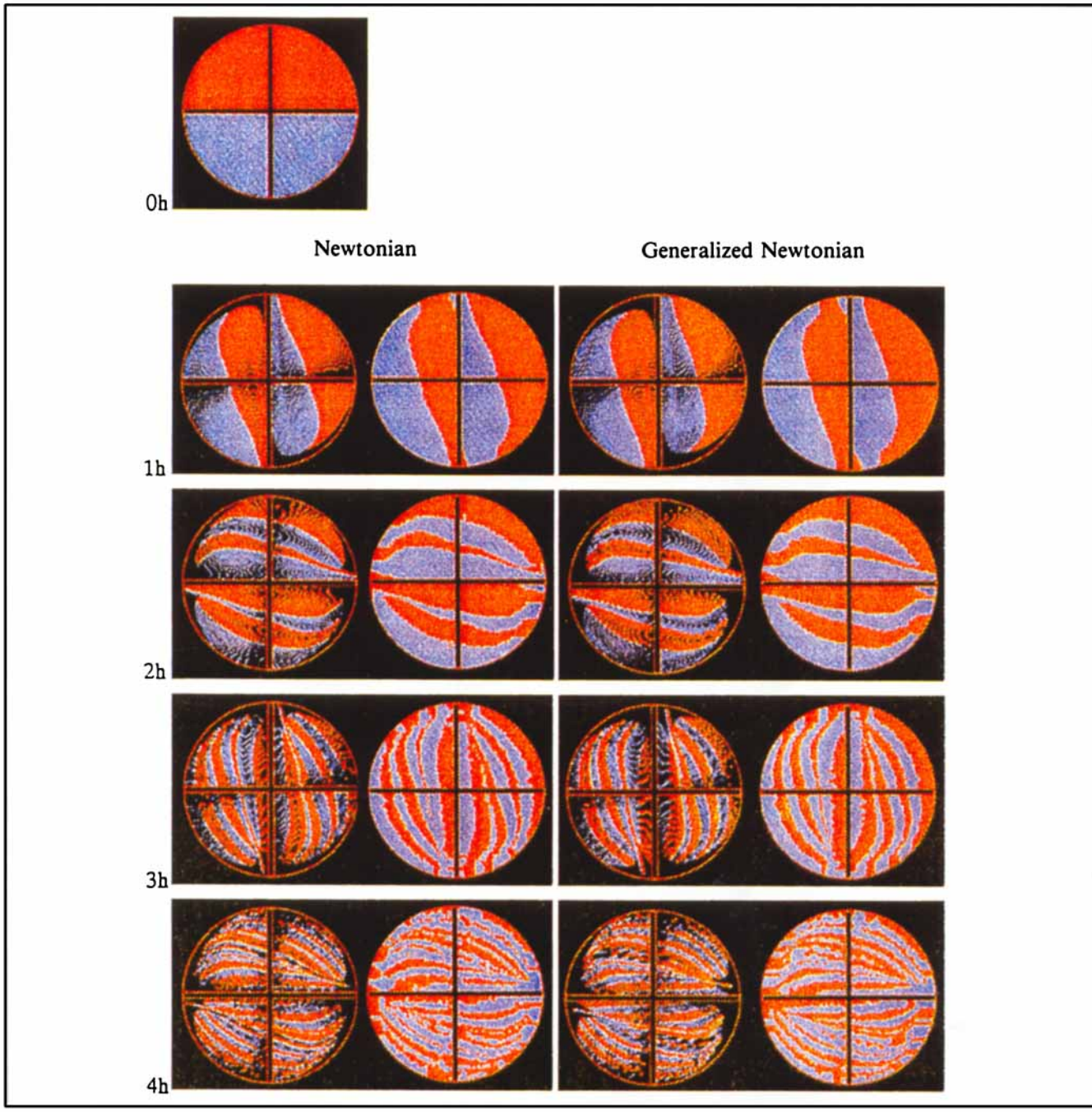

Figure 10. Concentration field at every change of blade for the Newtonian and the generalized Newtonian fluids.

The second and fourth columns have been fully colored by means of an interpolation algorithm.

generalized Newtonian fluid indicates that its velocity profile is flatter. This difference in velocity profile will have consequences on the statistical evaluation of the mixing process.

For our calculations, we select a grid of 100×100 material points in a cross section coinciding with a change of blade; 7,656 of these points are actually located in the fluid region. The pathlines and the mixing variables associated with these points are calculated over four blades of length h. Files containing material coordinates and mixing variables are recorded for every axial increment of $h/8$. We alluded earlier to the loss of accuracy due to the coarseness of the mesh, which causes particles to cross the walls. In the present analysis, 25% of the material points are lost before the end of the fourth blade. In the sixth section we will show that the use of a denser mesh reduces the loss of material points. Figure 9 identifies, in the entry section, the material points that will be maintained in the mixer up to $z = 4h$ and those that will be eliminated by passing through the walls. We observe that the material particles near the cylindrical boundary are the most likely ones to be eliminated.

Figure 10 compares the evolution of the concentration field for both fluids and with two types of shading. We start in the

Figure 11. Experimental vs. numerical results in successive cross sections covering four blades.

entry section with well separated red and blue fluids. The first and the third column are obtained by coloring the actual location of the material points without image treatment; we note in particular black zones in the neighborhood of the outer wall and at the intersection between the blades and the cylindrical boundary. The second and fourth columns make use of an interpolation algorithm to fill the black spots; any black spot will be colored according to the average color of its neighbors. It is clear that the interpolation scheme may affect the aspect of the concentration field near the walls while it is well preserved inside the flow. The successive rows of Figure 10 show the concentration field at the changes of blade; the first two columns correspond to a Newtonian fluid, the last two to the generalized Newtonian one. It is found that the concentration is little affected by changing the power index from 1 to 0.4.

A comparison between experimental and numerical results is shown in Figure 11; the cross sections correspond to axial coordinates equal to $(2k+1)h/8$, $0 \le k \le 15$. The comparison is based on the generalized Newtonian fluid. We observe a generally good agreement between experimental and theoretical results, despite the relative coarseness of the finite-element mesh. Although all gross features are well reproduced, there are differences in details that may be due to numerical errors as well as to nonperfect blades in the experiment that slip along the walls.

On the basis of the concentration field, it is possible to calculate the axial evolution of the segregation scale (Danckwerts, 1951) as explained in our first article (Avalosse and Crochet, 1997). For the correlation function, we have selected 100 intervals up to a maximum distance of 60 mm and 200 pairs of points selected at random for each interval. We observe in Figure 12 the exponential decrease of the segregation scale that is very similar for the Newtonian and the generalized Newtonian fluids. We cannot calculate the segregation scale beyond the fourth blade because its value lies below the characteristic size of the cells of our grid. It is interesting to compare the curves of Figure 12 with the results of

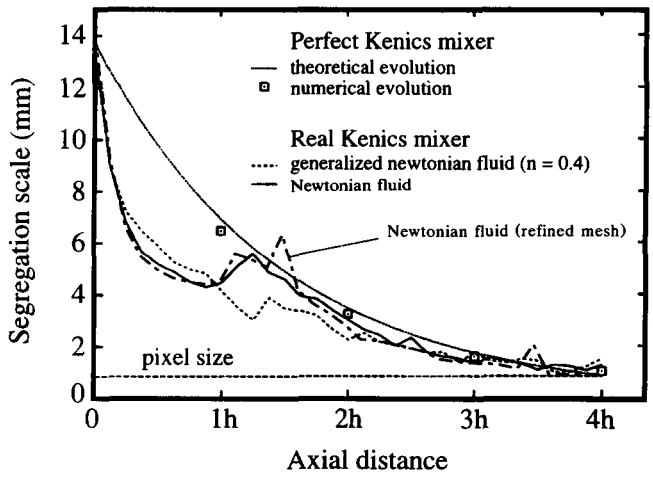

Figure 12. Axial evolution of the segregation scale for the Newtonian and the generalized Newtonian fluids.

The upper dotted curve corresponds to the ideal mixing of Figure 2.

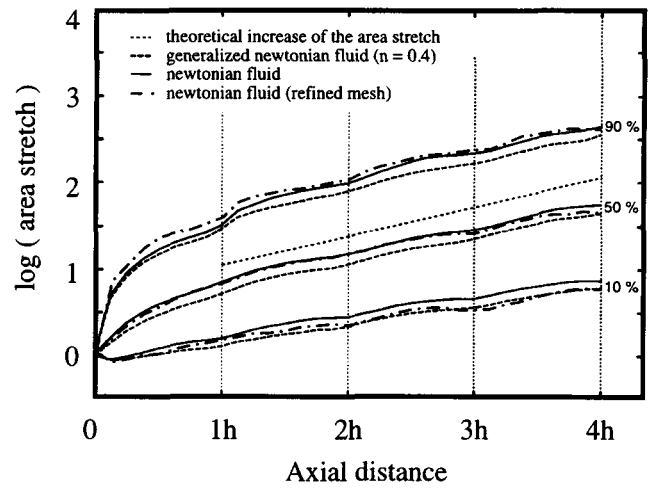

Figure 13. Axial evolution of the percentiles of the logarithm of the area stretch for the Newtonian and generalized Newtonian fluids.

the "perfect" mixer that would induce exponential striation as shown in Figure 2. The squares indicated in Figure 12 are obtained by applying to Figure 2 the same numerical treatment as for the finite-element analysis. The segregation scale is divided by two after every blade and corresponds to the half thickness of the strias. The dotted theoretical curve follows the law

$$S(z) = S(0)/2^{z/h}; \tag{11}$$

$S(0)$ is the segregation scale in the entry section (13.8 mm) and h is the axial length of a blade (115 mm). It is found that the actual segregation scale follows closely the ideal one beyond the first blade.

Figure 13 shows the axial evolution of the logarithm of the area stretch η by means of percentiles for the Newtonian and the generalized Newtonian fluids that exhibit very little difference. One finds an exponential growth of η as a function of the axial coordinate z. In Figure 13 we have also plotted the curve corresponding to the ideal mixing of Figure 2; one finds that this curve and the 50th percentile show the same slope, thus indicating the same interfacial growth.

The instantaneous efficiency as a function of the axial coordinate z is shown in Figure 14a; the results are very similar for the Newtonian and the generalized Newtonian fluids. The curves are almost periodic after the first blade, once the memory of the initial orientation is essentially forgotten. One observes a decrease of e_η before the blade change, immediately followed by a rapid growth, which shows the effect of slicing the fluid in two parts. Figure 14b shows the evolution of the time-averaged efficiency with a positive asymptotic value for the three percentiles shown in the figure. After one blade, one finds that only 10% of the material points exhibit a negative time-averaged efficiency. The asymptotic values of $\langle e_\eta \rangle$ are somewhat higher for the generalized Newtonian fluid.

Finally, Figure 15 shows the evolution of the residence time as a function of the axial coordinate. The difference between the 10th and 90th percentiles is somewhat larger for the Newtonian fluid than for the generalized Newtonian one. This

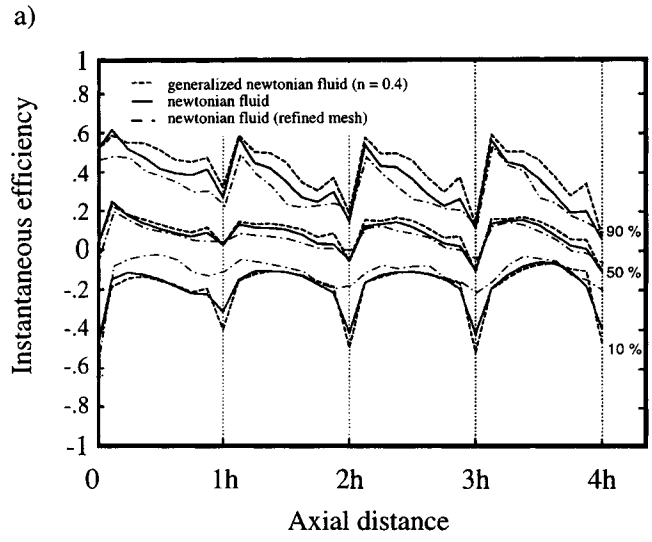

Figure 14. Axial evolution of the percentiles of the instantaneous efficiency e_η and the time-averaged efficiency $\langle e_\eta \rangle$ for the Newtonian and the generalized Newtonian fluids.

is due to the flatter velocity profile of the latter. However, the 90th percentile, which corresponds to higher values of the residence time, should be questioned because most points are located near the cylindrical wall where the accuracy is low.

Accuracy

In view of the loss of 25% of the material points through the walls of the mixer, we have recalculated the flow on a finer 3-D mesh, with the slightly different assumption that the blades now have a vanishing thickness. The new cross section is shown in Figure 16. There are 28 layers of elements in the axial direction instead of the 20 in Figure 7. Instead of triquadratic velocity–trilinear pressure elements, we use the enriched trilinear velocity–constant pressure element of Fortin (1981). The new mesh gives rise to 5,376 nodal pressures (instead of 2,436) and 68,487 nodal velocity components

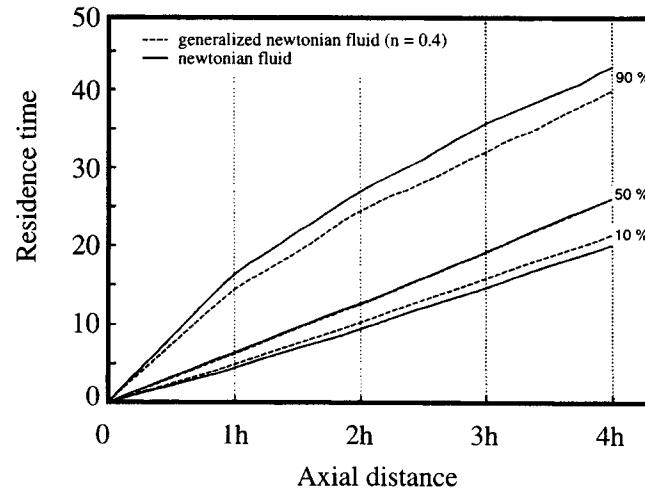

Figure 15. Axial evolution of the percentiles of the residence time for the Newtonian and the generalized Newtonian fluids.

(instead of 50,922). The total number of nodal variables has thus increased from 53,000 to 74,000. We have tracked 1,000 material points over a length of four blades, as in the previous section.

With the finer mesh, we now loose 20% of the material points instead of 25%. For the remaining points, we have calculated the segregation scale, the percentiles of the area stretch and of the efficiencies as a function of the axial distance for a Newtonian fluid. The segregation scale (Figure 12) is very similar for both meshes; some kinks may be due to the smaller number of pairs in the calculation of the segregation scale. The logarithm of the area stretch is essentially the same for both meshes, as shown in Figure 13. The instantaneous and averaged efficiencies, shown in Figure 14, are about

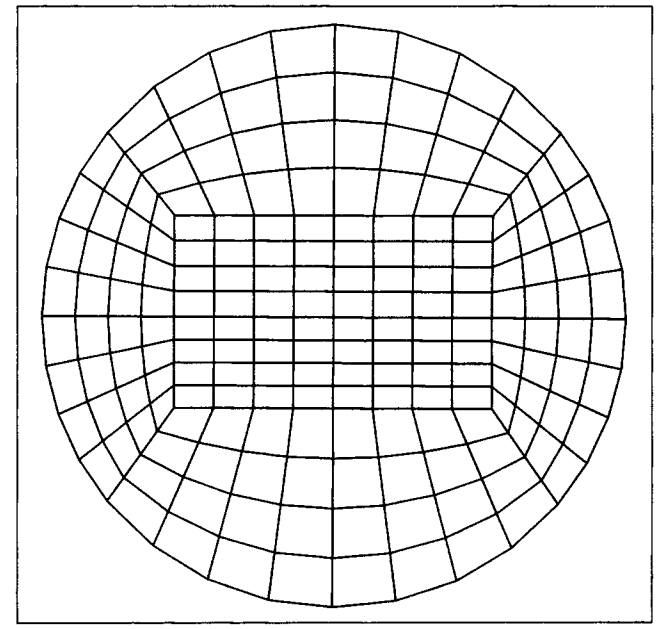

Figure 16. Cross section of the refined finite-element mesh.

the same for the 50th percentiles. However, larger deviations are observed for the 10th and 90th percentiles. The following may be an explanation. For particles moving near the walls, the efficiency is usually small (between -0.05 and 0.05). Since we loose a smaller number of points through the walls, we increase the number of those with a small efficiency. We would thus expect to obtain a higher curve for the 10th percentile (where the efficiency is negative) and a lower one for the 50th and 90th percentiles, where the efficiency is positive.

Conclusions

We have applied the numerical evaluation of mixing parameters based on a finite-element analysis to a 3-D problem. Despite the relative coarseness of the mesh and the associated discretization error, we have found good agreement between numerical results and experimental observations.

To assert the quality of mixing we have also shown that the simulation allows us to evaluate in detail a number of interesting parameters. In particular, we have found here that the amount of interface in the actual Kenics mixer follows closely the results of an ideal slicing mixer. We have also found that, for the Kenics mixer, the rheological properties of the fluids have little influence on the quality of the final mixture.

The central problem for further developments remains the accuracy of the calculations. We have used two meshes, with an increase of 40% of nodal variables for the second one. We have found that the number of "lost" particles decreases from 25% to 20%. It is clear that much more refined meshes would be needed for complex 3-D geometries, such as those encountered in twin-screw extruders (Avalosse, 1994).

Acknowledgments

One of the authors (Th. A.) gratefully acknowledges the support of Solvay s.a. The work of the other author (M.J.C.) was performed within the framework of Interuniversity Attraction Poles initiated by the Belgian State, Prime Minister's Office.

Literature Cited

Avalosse, Th., "Simulation Numérique du Mélange Laminaire par Eléments Finis," PhD Thesis, Université Catholique de Louvain, Louvain-la-Neuve, Belgium (1994).

Avalosse, Th., and M. J. Crochet, "Finite Element Simulation of Mixing; Part 1: Two-Dimensional Flow in Periodic Geometry," *AIChE J.*, **43**(3), 577 (1997).

Danckwerts, P. V., "The Definition and Measurement of Some Characteristics of Mixtures," *Appl. Sci. Res.*, *A*, **3**, 279 (1951).

Fortin, M., "Old and New Finite Elements for Incompressible Flows," *Int. J. Numer. Methods fluids*, **1**, 347 (1981).

Goublomme, A., B. Draily, and M. J. Crochet, "Numerical Prediction of Extrudate Swell of a High-Density Polyethylene," *J. Non-Newtonian Fluid Mech.*, **44**, 171 (1992).

Khakkar, D. V., J. G. Franjione, and J. M. Ottino, "A Case Study of Chaotic Mixing in Deterministic Flows: the Partitioned-Pipe Mixer," *Chem. Eng. Sci.*, **42**, 2909 (1987).

Ling, F. H., "Chaotic Mixing in the Kenics Static Mixer," *ANTEC '95*, p. 130 (1995).

Middleman, S., *Fundamentals of Polymer Processing*, McGraw-Hill, New York, p. 327 (1977).

Ottino, J. M., 1989, *The Kinematics of Mixing: Stretching, Chaos, and Transport*, Cambridge University Press, New York (1989).

Souvaliotis, A., S. C. Jana, and J. M. Ottino, "Potentialities and Limitations of Mixing Simulations," *AIChE J.*, **41**, 1605 (1995).

Tanguy, P. A., R. Lacroix, F. Bertrand, L. Choplin, and E. Brito de la Fuente, "Finite Element Analysis of Viscous Mixing with a Helical Ribbon-Screw Impeller," *AIChE J.*, **38**, 939 (1992).

Manuscript received Sept. 25, 1995, and revision received Sept. 30, 1996.